Received: August 14, 2024 | Revised: November 1, 2024 | Accepted: November 4, 2024

JOURNAL OF APPLIED RESEARCH ON SCIENCE AND TECHNOLOGY
JARST
INSTITUTE OF RESEARCH AND DEVELOPMENT
RAJAMANGALA UNIVERSITY OF TECHNOLOGY THANYABURI
ISSN ONLINE: 2773-9473
https://ph01.tci-thaijo.org/index.php/rmutt-journal

Effectiveness of separated ICR for a wheeled skid-steering robot

Ditsakorn Wanichratanagul, Witaya Wannasuphoprasit and Viboon Sangveraphunsiri*

Department of Mechanical Engineering, Faculty of Engineering, Chulalongkorn University, Bangkok 10330, THAILAND
*Corresponding author: viboon.s@chula.ac.th

ABSTRACT

The skid-steering robot has gained popularity due to its mechanical simplicity and robustness, making it a preferred choice in various applications. However, this configuration is prone to slip during turning maneuvers, resulting in inaccurate trajectory prediction using the conventional differential drive kinematic model. The separated instantaneous centers of rotation (ICRs) approach has been proposed to address this issue and mitigate slips experienced during turns. Compared to the computer simulations, this study investigates the trends of the separated ICR approach on the trajectory error using a real-world robot across different terrains in low dynamic conditions. The findings reveal that the effectiveness of the separated ICR approach in compensating for slip varies depending on the turning radius. Specifically, the approach is less effective with smaller turning radii and vice versa. Surprisingly, the terrain type does not significantly impact the effectiveness of the separated ICRs approach, suggesting that its performance is more closely linked to the turning radius than to the terrain conditions. Although the simulation method outlined in this research struggles with precise surface roughness estimation, it demonstrates consistent skid behavior, indicating the potential utility of separated ICRs for skid-steering robots. To enhance the accuracy of computer simulations, a deeper exploration of terrain surface conditions is necessary. Nonetheless, the implementation of separated ICRs on our four-wheel mobile robot shows promising results, underscoring the viability of using separated ICRs to improve the performance of skid-steering robots in various settings.

Keywords: Ground vehicles, Four-wheel mobile robot, Kinematics, Skid-steering, Instantaneous center of rotation

INTRODUCTION

Skid-steering robots have become increasingly popular in outdoor environments due to their mechanical simplicity and robustness, allowing more space within the robot [1, 2]. This type of robot has various applications especially in uneven terrain or dangerous missions, for example, mining robots [3], agricultural robots [4, 5], Planetary exploration robots [6], surveillance robots [7], and security robots [8]. The main focus of this project is to develop an autonomous outdoor mobile robot for transporting objects between buildings on a university campus.

The maneuvering configuration is based on the relative velocity of the left and right-side drive, similar to the unicycle differential-drive configuration. However, slip is inevitable during the turning maneuver due to the configuration involving multiple wheels or a track on both sides [9]. The slip violates the differential drive's no-slip and pure rolling assumption and is the primary challenge of the skid-steering configuration [10, 11].

Kinematic models based on differential drive configuration have been proposed to deal with slip. Among those, the most popular approach is the separated instantaneous center of rotation (ICR), which focuses on the ICRs of each side of the wheels instead of the configuration ICR. The separated ICR uses the length between the ICR of each side, which is obtained from the experiment, instead of the wheel-to-wheel width in the differential drive kinematic model. The previous works experiment with this approach using a thread robot [12] and a 4-wheel skid-steering robot [13], which gives better dead reckoning results than the differential drive kinematic model.

In contrast to the configuration ICR that varies considerably depending on the configuration and ground contact dynamics, the separated ICR remains within bounded regions of each side of the robot at low speed on hard terrain as the inertia force is the main contributor [14, 15]. Thus, the approximately constant position of the wheel ICRs can be assumed for each configuration.

This research aims to discover the trends of the separated ICR approach in terms of trajectory error compared to the typical differential drive kinematic model on a robot with real-time position tracking. The study tests the robot over 4 different terrains and 2 different turning radii, which are the actual applications of this project robot.

DOI: 10.60101/jarst.2024.257672

JOURNAL OF APPLIED RESEARCH ON SCIENCE AND TECHNOLOGY

MATERIALS AND METHODS

The setup of skid-steering in this research is depicted in Figure 1, which consists of two pairs of non-steering wheels at the front and rear of the robot. The linear and angular velocities of the robot (v,ω) is dictated by the velocities of the left and the right-side wheels (v_l, v_r). Each side's front and rear wheels must rotate at the same speed. To investigate the violation of the pure rolling and no-slip assumption, each wheel is defined by four constant parameters as α,β,l,r along with an angular variable $\varphi(t)$, as illustrated in Figure 2. Each wheel's longitudinal and lateral velocity can be expressed in Eq. (1) and (2).

$$\left[-\sin(\alpha+\beta)\ \cos(\alpha+\beta)\ l\cos\beta\right]R(\theta)v + r\dot{\varphi} = 0 \quad (1)$$

$$\left[\cos(\alpha+\beta)\ \sin(\alpha+\beta)\ l\sin\beta\right]R(\theta)v = 0 \quad (2)$$

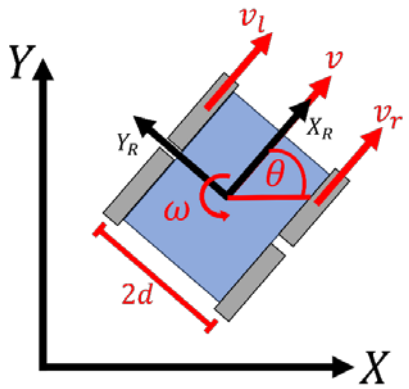

Figure 1 skid steering configuration with two pairs of non-steering wheels at the front and rear of the robot.

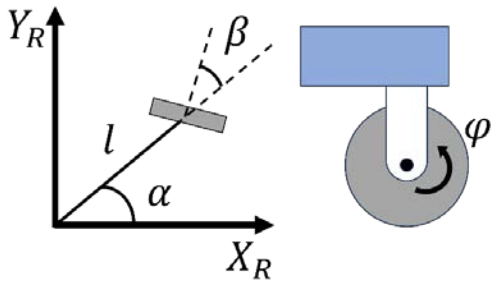

Figure 2 non-steering wheel configuration.

Where $R(\theta)$ represents the configuration rotation matrix, and v represents the configuration velocity vector. The lateral velocity is investigated further since it has to remain zero during the turning maneuver to satisfy the no-slip and pure rolling assumption. The lateral velocity of every wheel in this research configuration is defined in Eq. (3).

$$C_R R(\theta)v = 0 \quad (3)$$

While C_R is a 4x3 matrix containing the wheel configuration term of every wheel. Obviously, for skid configuration, rank $C_R = 2$ due to its two rotation axles parallel to each other. This serves as proof that the skid configuration could not steer without violating the no-slip and pure rolling assumption[9].

Unlike the skid configuration, the differential drive, which has a similar configuration, is steerable without violating any of those assumptions. The inverse kinematics of the differential drive can be expressed as follows[16]:

$$\begin{bmatrix} v_l \\ v_r \end{bmatrix} = \begin{bmatrix} 1 & -d \\ 1 & d \end{bmatrix} \begin{bmatrix} v \\ \omega \end{bmatrix} \quad (4)$$

where d represents the distance from the center line to each side of the mobile robot wheels. However, unlike the differential drive, which does not generate slip, Eq. (4) fails to accurately predict the motion of the skid configuration during turning maneuvers. Separate ICRs are employed to minimize motion errors. By treating each side of the wheels as rigid bodies, there are three ICRs within the configurations:

$ICR_C = (x_c, y_c)$ for overall configuration ICR, $ICR_L = (x_l, y_l)$ for left-side wheels ICR and $ICR_R = (x_r, y_r)$ for right-side wheels ICR as shown in Figure 3 [12, 13].

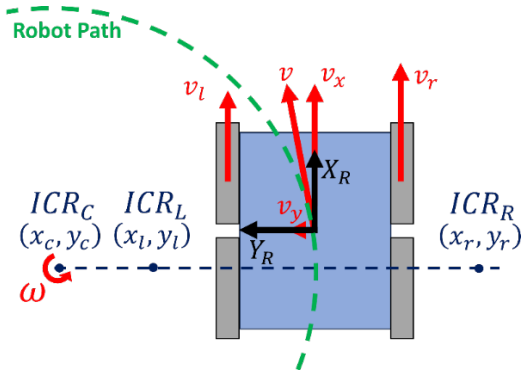

Figure 3 Separated ICRs of both sides of the configuration and ICR of the whole configuration when the configuration turns along the path.

Considering that both sides of the configuration rotate around their respective ICR, the location of each ICR can be shown as follows:

$$y_c = -\frac{v_x}{\omega} \quad (5)$$

$$y_l = \frac{v_l - v_x}{\omega} \quad (6)$$

$$y_r = \frac{v_r - v_x}{\omega} \quad (7)$$

$$x_c = x_l = x_r = \frac{v_y}{\omega} \quad (8)$$

Assume that the configuration is symmetrical, and its center of gravity is placed at the center of the

DOI: 10.60101/jarst.2024.257672

JOURNAL OF APPLIED RESEARCH ON SCIENCE AND TECHNOLOGY

configuration, the longitudinal velocity of the configuration becomes zero:

$$x_c = x_l = x_r = 0 \tag{9}$$

Assume that the mass of the configuration is well distributed over its body, the displacement between the ICR of each side and the configuration in the y-axis should be the same:

$$y_l = -y_r = y_o \tag{10}$$

Where y_0 is the displacement between the wheel ICR of both sides to the center of the configuration in the y-axis. The inverse kinematic model of the skid steering configuration can be expressed as follows:

$$\begin{bmatrix} v_l \\ v_r \end{bmatrix} = \begin{bmatrix} 1 & -y_0 \\ 1 & y_0 \end{bmatrix} \begin{bmatrix} v \\ \omega \end{bmatrix} \tag{11}$$

The value of y_0 can be determined by measuring the steering efficiency of the configuration through experimentation. By performing the zero-radius turning and comparing the actual angle and the angle, the configuration should be based on wheel rotation; the value of y_0 can be shown as follows.

$$y_0 = \frac{\int v_r dt - \int v_l dt}{2\theta} \tag{12}$$

Also, in low speed, y_0 is significantly dependent on the robot configuration parameters. External variables such as terrain type exert negligible influence on its values [14].

Skid steering robot

Figure 4 depicts the skid steering robot employed in this research, which operates as a four-wheel drive system. Its dimensions (W×L×H) are $0.71 \times 0.78 \times 0.54\,m$ and weight approximately $48\,kg$. The robot is powered by electricity stored in onboard batteries, the robot's locomotion is facilitated by four brushless servo motors, each fitted with encoders attached to its respective wheel. The distance between the center of the left and the right-side wheels d is $0.57\,m$. Suspension modules are incorporated at each wheel to mitigate force transmission from the ground to the robot body. This feature enables the robot to navigate uneven terrain smoothly, as illustrated in Figure 5. Additionally, to prove that the robot could overcome the friction generated by the nature of the skid-steering, the robot can perform a 180-degree turn utilizing a kinematic model derived from Eq. (4), using remote control, as demonstrated in Figure 6. The robot has a ZED2 stereo camera with a built-in V-SLAM algorithm (Visual Simultaneous Localization and Mapping). The camera observes the position of the environment feature point based on the parallax distance between each lens. The zalgorithm uses this information with IMU to map the environment and localize the camera to the map simultaneously to record the camera's trajectory. Eq. (4) and (11) are incorporated into the robot's control algorithm to conduct the experimental study.

Figure 4 Skid steering robot in this project.

Figure 5 Snapshot of robot moving on uneven terrain.

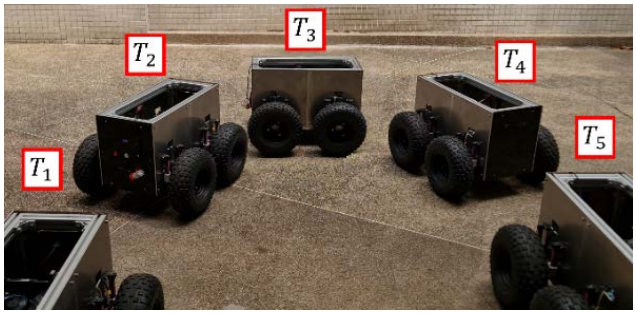

Figure 6 Snapshot of robot performs 180-degree turn indicates that the robot can overcome friction and perform skid-steering behavior.

Experiment methodology

The experiment takes place on four different terrains based on the campus, which are this project's main operation areas: a grass field, a ceramic plate floor, a concrete road, and a gravel passageway, as illustrated in Figure 7. The experiment was conducted in each terrain by letting the skid-steering robot perform 180-degree U-turns with 2 different radii, 1 and 2 meters. On each terrain and each radius, experimented using 2 different control algorithms, Eq. (4) and Eq. (11). The robot has to maintain linear velocity $1\,m/s$ during the experiment. The trajectory of each experiment is collected by a ZED2i stereo camera using its built-in V-SLAM algorithm. Due to the insensitivity over the terrain of the y_0, the experiment to determine y_0 is conducted over a gravel passageway and will use the

DOI: 10.60101/jarst.2024.257672

value on all the 180-degree turning experiments and simulations. Note that the ZED2i stereo camera is factory-calibrated and used as is.

Dynamic simulation

This study uses MATLAB's SimScape to simulate the skid steering trajectory. The SimScape model is shown in Figure 8. The model is constructed from robot configurations mentioned above to simulate joint-to-joint simulation as shown in Figure 8 section 1. The model wheels receive velocity input from Figure 8 section 2 and calculate force interaction, including friction, which generates slip in case fiction is insufficient using the contract force library [17] in Figure 8 section 3. This model has conducted a 180-degree turn using experiment conditions beforehand to investigate the friction coefficient. By varying the friction coefficient, the trajectory results of each experiment do not show any significant difference. Hence, we choose the friction coefficient 0.9 to represent the simulation result in the next topic.

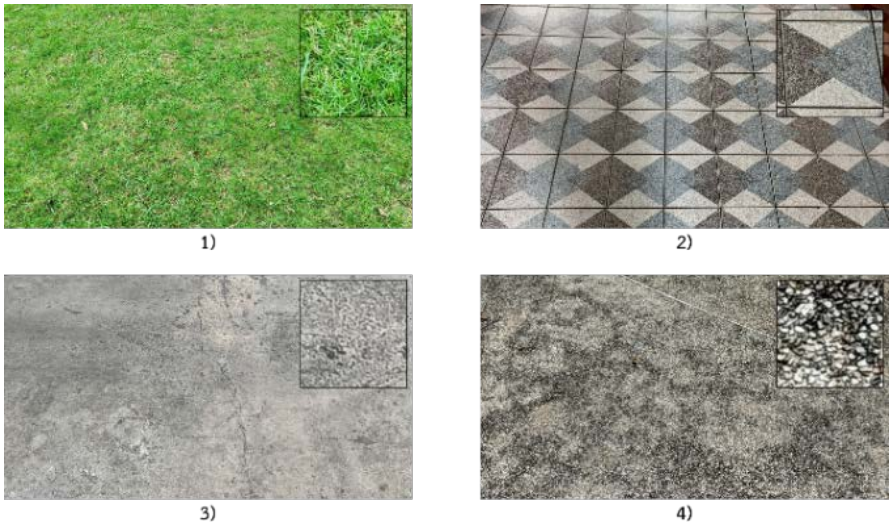

Figure 7 Urban terrain used in experiment 1) grass field 2) ceramic floor 3) concrete road 4) gravel passageway.

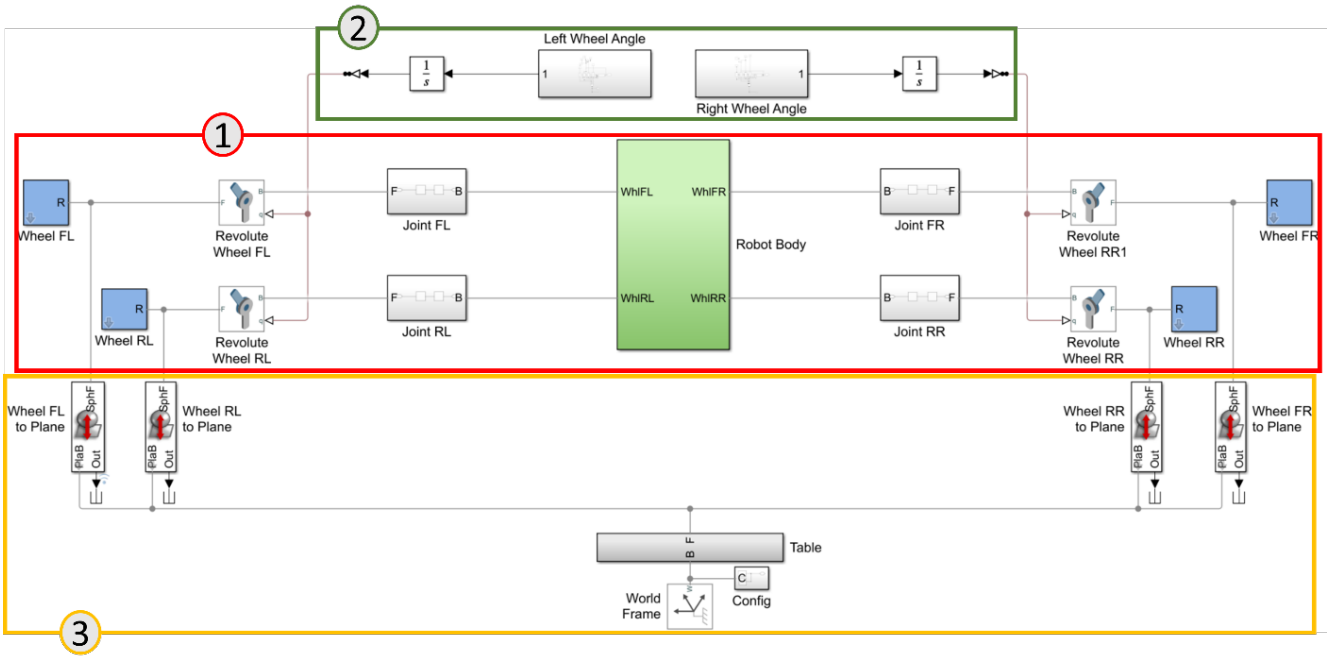

Figure 8 MATLAB's SimScape model for skid steering configuration moving on the floor with adjustable friction coefficient.

RESULTS AND DISCUSSION

By performing the zero-radius turning experiment on the gravel passageway, we obtain $y_o = 0.93\,m$ and use this value in the 180-degree turning experiments. The trajectory of the 180-degree turning experiment on four terrains at a radius of 1 and 2 meters is depicted in Figures 9 and 10, respectively. The continuous lines indicate the trajectory of the robot using Eq. (4) (using a constant d) as the robot algorithm, and the dashed lines indicate the trajectory of the robot using Eq. (11)

DOI: 10.60101/jarst.2024.257672

JOURNAL OF APPLIED RESEARCH ON SCIENCE AND TECHNOLOGY

(using a constant y_0) as the robot algorithm. The green line indicates the reference trajectory, the blue line denotes the simulation trajectory, and the other colors show the robot's trajectories on different terrains.

The trajectories of the robot using Eq. (11) converge to the reference trajectory more than the trajectories using Eq. (4) in both turning radii and the trajectories that use the same algorithm seem to converge with each other, which will be investigated further. All the experiment trajectories are shorter than the reference trajectory in which the 2 meters radius trajectories are closer to the reference than the other, which indicates that all the experiment trajectories are slip. However, the larger radius generates a smaller slip, and the Eq. (11) algorithm can reduce the trajectory error but cannot reduce the slip.

The simulation can simulate skid-steering behavior with Eq. (11) trajectories that converge more to the reference than the other in both turning radii, as found in the experiment trajectories. The simulation trajectories fail to simulate accurate slip, as evidenced by the longer distance between the simulation trajectories and the experiment. The friction model of the simulation is the main suspect of the inaccurate slip in the simulation as the model does not consider the wheel deformation.

To investigate furthermore about error comparison between both turning radii, the normalized error of each trajectory can be analyzed by calculating the distance between the experimental trajectory and the reference trajectory at the corresponding time, then normalizing it by dividing by the radius of the turning curve, as stated in Eq. (13). The errors of the trajectory depicted in Figure 9 and Figure 10 are presented in Figure 11 and Figure 12 respectively. Note that simulation results are excluded due to their accuracy.

$$error_t = \frac{\sqrt{\left(x_{ref,t} - x_{actual,t}\right)^2 + \left(y_{ref,t} - y_{actual,t}\right)^2}}{radius} \qquad (13)$$

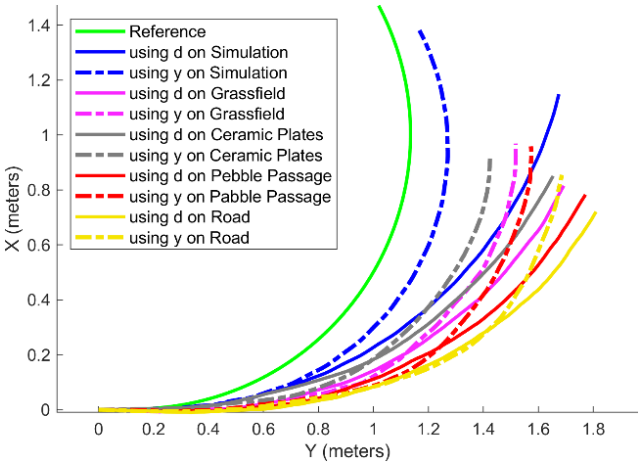

Figure 7 Trajectory results of the experiment on different terrain at a radius of 1 meter.

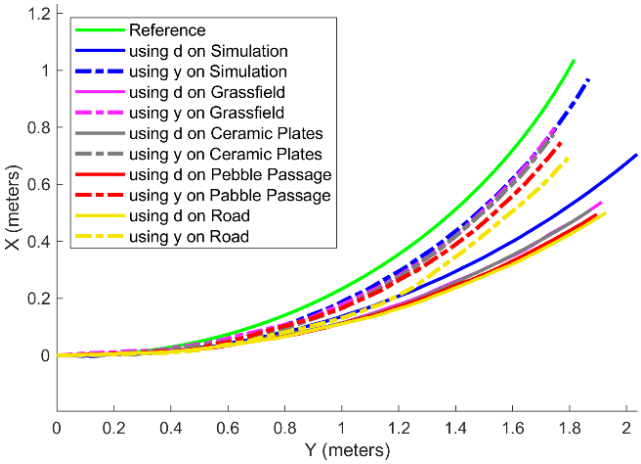

Figure 10 Trajectory results of the experiment on different terrain at a radius of 2 meters.

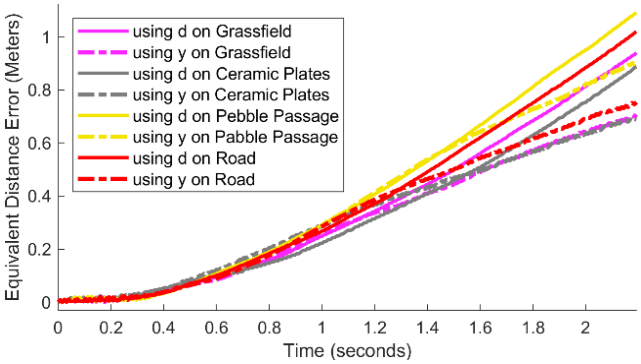

Figure 11 Equivalent trajectory error of the experiment on different terrain at a radius of 1 meter.

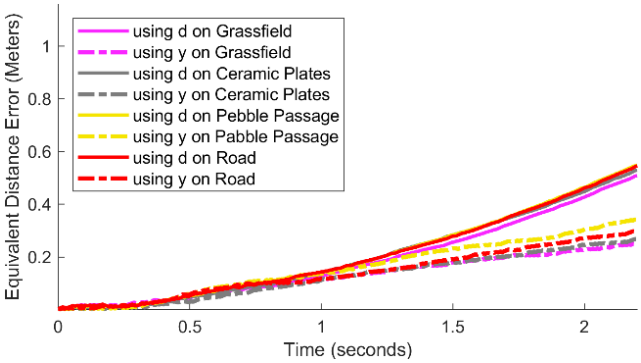

Figure 12 Equivalent trajectory error of the experiment on different terrain at a radius of 2 meters.

From Figures 11 and 12, the yellow dashed line in Figure 11 shows the trajectories using Eq. (11) have less error than the trajectories using Eq. (4) in both turning radii as the slopes are lower and the final errors are also more minor which indicates that the. The equivalent errors of the experiment with a larger radius are smaller than those with a smaller radius, which also supports that turning with a larger radius generates a smaller slip. In each turning radii, the trajectory errors of each algorithm are adhering together, which indicates that the terrain types are insignificant to slip behavior in this project setup as the parameter y_0 is mainly influenced by the robot configuration at low speed,

DOI: 10.60101/jarst.2024.257672

which can apply to the other robot in low dynamic operation.

The dashed lines and continuous lines between 0 - 0.8 second in Figure 11 and between 0 - 0.5 seconds in Figure 12 are aligned to indicate the angular acceleration period. The yellow dash line in Figure 11 has a more extended acceleration period. The gravel passageway is suspected to be the most friction terrain, which makes the robot more influenced by the dynamic conditions, and so is the y_0.

Compared to the robot size, the separated ICR approach significantly reduces trajectory error in low dynamic conditions such as large turning radius. The compensated control strategy, increasing the trajectory duration to match the reference, is recommended to reduce the trajectory error further. Also, a more accurate wheel-ground interaction model is recommended to simulate behavior precisely.

CONCLUSIONS

This study demonstrates the efficacy of the separated ICR approach on the actual condition that the robot in this research has to operate. Skid behavior trends have less impact when the robot turns at a larger radius. The trajectory error is also smaller when using a separate ICR approach, but the approach does not reduce the slip at each wheel. The experiment is done over 4 terrains with different friction coefficients and characteristics. The result shows that the terrain type is insignificant to the skid behavior in low dynamic. The simulation proposed in this research can replicate the skid behavior but fails to predict the trajectories accurately. The interaction between the wheel and the ground is the leading cause of the inaccuracy of the simulation. Despite the trajectory errors, the separated ICR approach is recommended to compensate for slip in low dynamic conditions. More sophisticated control strategies for trajectory timing adjustment and travel length compensation can also be considered in the future.

REFERENCES

1. Wang T, Wu Y, Liang J, Han C, Chen J, Zhao Q. Analysis and Experimental Kinematics of a Skid-Steering Wheeled Robot Based on a Laser Scanner Sensor. Sensors [Internet]. 2015;15(5):9681-702. Available from: https://doi.org/10.3390/s150509681.
2. Maclaurin B. Comparing the steering performances of skid- and Ackermann-steered vehicles. Proceedings of the Institution of Mechanical Engineers Part D Journal of Automobile Engineering. 2008;222:739-56.
3. Huh S, Lee U, Shim H, Park JB, Noh JH, editors. Development of an unmanned coal mining robot and a tele-operation system. 2011 11th International Conference on Control, Automation and Systems; 2011 Oct 26-29.
4. Fernandez B, Herrera PJ, Cerrada JA. A Simplified optimal path following controller for an agricultural skid-steering robot. IEEE Access. 2019;7:95932-40.
5. Cheein FAA, Carelli R. Agricultural robotics: Unmanned robotic service units in agricultural tasks. IEEE Industrial Electronics Magazine. 2013; 7(3):48-58.
6. Liu G, Liu Y, Zhang H, Gao X, Yuan J, Zheng W. The kapvik robotic mast: An innovative onboard robotic arm for planetary exploration rovers. IEEE Robotics & Automation Magazine. 2015;22(1): 34-44.
7. Zhang C, Zhan Q, Wang Q, Wu H, He T, An Y. Autonomous dam surveillance robot system based on multi-sensor fusion. Sensors [Internet]. 2020; 20(4):1097. Available from: https://doi.org/10.3390/s20041097.
8. Mandow A, Serón J, Pastor F, García-Cerezo A. Experimental Validation of a Robotic Stretcher for Casualty Evacuation in a Man-Made Disaster Exercise. In: 2020 IEEE International Symposium on Safety, Security, and Rescue Robotics (SSRR); 2020 Nov 4-6. Abu Dhabi, UAE. p. 241-5.
9. Campion G, Bastin G, Dandrea-Novel B. Structural properties and classification of kinematic and dynamic models of wheeled mobile robots. IEEE Transactions on Robotics and Automation. 1996; 12(1):47-62.
10. Yi J, Wang H, Zhang J, Song D, Jayasuriya S, Liu J. Kinematic modeling and analysis of skid-steered mobile robots with applications to low-cost inertial-measurement-unit-based motion estimation. IEEE Transactions on Robotics. 2009;25(5):1087-97.
11. Burke M. Path-following control of a velocity constrained tracked vehicle incorporating adaptive slip estimation. In: 2012 IEEE International Conference on Robotics and Automation; 2012 May 14-18. Minnesota, USA. p. 97-102.
12. Martínez J, Mandow A, Morales J, Pedraza S, Garcia A. Approximating kinematics for tracked mobile robots. The International Journal of Robotics Research. 2005;24:867-78.
13. Mandow A, Martinez JL, Morales J, Blanco JL, Garcia-Cerezo A, Gonzalez J. Experimental kinematics for wheeled skid-steer mobile robots. In: Proceedings of the 2007 IEEE/RSJ International Conference on Intelligent Robots and Systems. 2007 Oct 29 - Nov 2; San Diego, CA, USA. p. 1222-7.

DOI: 10.60101/jarst.2024.257672

JOURNAL OF APPLIED RESEARCH ON SCIENCE AND TECHNOLOGY

14. Góra K, Kujawinski M, Wroński D, Granosik G. Comparison of energy prediction algorithms for differential and skid-steer drive mobile robots on different ground surfaces. Energies. 2021;14(20): 6722.

15. Martínez JL, Morales J, García JM, García-Cerezo A. Analysis of tread ICRs for wheeled skid-steer vehicles on inclined terrain. IEEE Access. 2023; 11:547-55.

16. Eiammanussakul T. Design and Development of a Wall Climbing Robot with Magnetic Wheels: Chulalongkorn University; 2013.

17. Miller S. Simscape Multibody Contact Forces Library [Internet]. San Francisco: GitHub; 2014 [updated 2023 Dec 07; cited 2024 Jul 17]. Availability from: https://github.com/mathworks/Simscape-Multibody-Contact-Forces-Library.

DOI: 10.60101/jarst.2024.257672